Research Square

Preprints are preliminary reports that have not undergone peer review.
They should not be considered conclusive, used to inform clinical practice,
or referenced by the media as validated information.

SBOA-GI: A Physics-Informed Enhancement of the Secretary Bird Optimization Algorithm for Gravity Inversion, with an Honest Assessment of Its Limits on Field Data from the Charak Salt-Dome Province, Zagros, Iran

Reza Toushmalani

r.toushmalani@iau.ac.ir

Islamic Azad University

Research Article

Keywords: Gravity inversion, Metaheuristic optimization, Secretary Bird Optimization Algorithm, Salt dome, Zagros, Non-uniqueness

Posted Date: November 10th, 2026

DOI: https://doi.org/10.21203/rs.3.rs-10863615/v1

License: This work is licensed under a Creative Commons Attribution 4.0 International License.
Read Full License

Additional Declarations: No competing interests reported.

Abstract

Metaheuristic optimization is now common for interpreting potential-field geophysical data, yet most published variants are validated only on noise-free synthetic models. This study introduces SBOA-GI, a creatively redesigned, physics-informed variant of the recently proposed Secretary Bird Optimization Algorithm (SBOA; Fu et al. 2024): rather than applying SBOA unmodified, we reconceive four of its five update rules around the ill-posedness, unequal parameter sensitivity, and depth–amplitude trade-off of gravity inversion — to our knowledge the first SBOA variant conceived for a potential-field inverse problem rather than generic benchmarks. The redesign combines Latin-hypercube/opposition-based initialization, self-adaptive differential mutation, sensitivity-weighted Lévy flight, a Lévy–Cauchy stagnation-escape mechanism, physically bounded exploitation with an embedded local Levenberg–Marquardt (LM) polish, and a shrinking-bound restart loop. SBOA-GI, standard SBOA, particle swarm optimization (PSO), and LM were compared on synthetic fault, sphere, and horizontal-cylinder models (0/5/10% Gaussian noise, 30 runs each) and on real Bouguer gravity data (875 stations) from two salt-dome anomalies near Charak, Zagros fold-thrust belt, Iran. At zero noise, SBOA-GI cut parameter RMSE roughly eleven orders of magnitude versus standard SBOA; the gain shrank to negligible at 5% noise and reversed at 10%, showing its refinements mainly speed convergence rather than raise the noise-limited accuracy ceiling. On real data, contrary to expectation, classical LM gave the lowest and most stable misfit (≈ 2.16 and ≈ 1.25 mGal RMS) at a fraction of the metaheuristics' cost, reflecting a smooth misfit surface and the well-known depth–amplitude trade-off. We report this transparently as evidence for the practical limits of metaheuristic enhancement in gravity inversion.

Article Highlights

- SBOA-GI cuts noise-free inversion error ~10^{11}-fold versus standard SBOA but not under high noise
- On real Charak salt-dome gravity data, classical Levenberg–Marquardt outperformed all tested metaheuristics
- Findings show metaheuristic gains are convergence-speed, not accuracy-ceiling, benefits on smooth misfit surfaces

1. Introduction

Gravity inversion — estimating the location, depth, and density contrast of subsurface bodies from surface gravity measurements — is an inherently ill-posed and non-unique problem: multiple geometrically distinct source distributions can reproduce the same observed anomaly to within measurement error (Blakely 1995). Because the misfit surface of such problems is frequently multimodal, population-based metaheuristic optimizers have progressively displaced purely gradient-based least-squares methods as the interpretation tool of choice over the last two decades.

Essa and co-workers established much of the groundwork for this shift, applying particle swarm optimization (PSO) and its modified variants to recover the depth, shape factor, and amplitude

coefficient of idealized causative bodies — spheres, horizontal cylinders, and vertical cylinders — from both synthetic and field gravity data, demonstrating that PSO variants can accurately recover source parameters under noise-free and noise-corrupted conditions. Subsequent work extended PSO-based inversion specifically to 2-D vertical-fault structures (Anderson, Essa & Elhussein 2020), showing that pre-filtering the anomaly with a horizontal-gradient filter improves recovery and validating the approach on field data from known faults, while more recent studies have hybridized PSO with the gravitational search algorithm to balance exploratory and exploitative capacity over faulted structures and to augment the recovered model with confidence intervals and correlation-based uncertainty analysis (Kumar et al. 2024).

A parallel line of metaheuristic development, disconnected from potential-field geophysics, has produced a rapidly growing family of bio-inspired global optimizers. Among these, Fu, Liu, Chen and He (2024) introduced the Secretary Bird Optimization Algorithm (SBOA), a population-based metaheuristic modeled on the hunting and predator-evasion behavior of the secretary bird, structuring its search into global exploration, local development, and convergence-reinforcement phases. Because SBOA is architecturally similar to the swarm-based inversion schemes already validated in gravity interpretation but has — to the best of our knowledge — not yet been benchmarked on a potential-field inverse problem, it offers a natural and previously untested candidate for this domain. Its original benchmarking against algorithms such as WOA, GWO, COA and DBO showed competitive performance on standard numerical test suites, though, consistent with the No-Free-Lunch theorem, no single optimizer is expected to dominate across all problem classes.

This motivates the central question of the present study: does a domain-informed enhancement of SBOA — incorporating structured initialization, adaptive mutation, sensitivity-aware step control, and a hybrid local–global refinement mechanism tailored to the geometry and noise characteristics of gravity data — provide a genuine, reproducible advantage over (i) unmodified SBOA, (ii) PSO, and (iii) classical Levenberg–Marquardt (LM) least-squares inversion, on both synthetic and real field data? We test this on data from the salt-diapir province of the Zagros fold-and-thrust belt in Iran, where numerous Hormuz-series salt bodies have risen through a thick sedimentary overburden to form domes, producing negative-density-contrast gravity anomalies of the type these idealized-body inversion techniques are designed to resolve. Unlike most published metaheuristic-inversion studies, which report only favorable outcomes, we adopt an explicitly falsifiable comparison protocol — identical population size and iteration budget across algorithms, 30 independent runs per condition — and commit in advance to reporting cases where the proposed enhancement fails to improve on its baseline.

The contribution of this work is threefold. First, we do not apply SBOA to gravity inversion as an off-the-shelf solver; we redesign four of its five update rules — initialization, both exploratory hunting sub-phases, and the exploitation phase — specifically to address pathologies known to affect potential-field inverse problems (a wide, poorly informative initial search bracket; parameters of very unequal sensitivity such as depth versus dip; and a shallow, elongated depth–amplitude trade-off valley rather than isolated local minima), rather than adopting generic, problem-agnostic improvements taken from the numerical-

optimization literature. Second, we couple this redesigned global search to a cheap, probabilistically triggered local Levenberg–Marquardt polish, so that SBOA-GI is best understood as a hybrid global–local scheme rather than a purely metaheuristic one. Third, and most important for the credibility of the comparison, we test this design on both synthetic and real field data and report, without adjustment after the fact, the specific noise regime and data type in which the added machinery does not pay for its computational cost — a negative result rarely disclosed in the metaheuristic-inversion literature.

1.1 Supplementary literature review

The expanding SBOA family and the gap addressed here. Since the publication of the Secretary Bird Optimization Algorithm as a three-phase hunting and predator-evasion metaheuristic (Fu et al. 2024), a rapidly growing family of enhanced variants has appeared, almost all validated only on standard benchmark suites and engineering design problems. ISBOA introduces hybrid chaotic mutation, an improved attacking-prey strategy, and population reconstruction (Yan & Ding 2025); a further improved variant combines circle-chaotic initialization, a differential evolution strategy, and a population-diversity mechanism (Qin et al. 2024); HS-SBOA couples iterative-mapping initialization, an adaptive weighting strategy, and Cauchy mutation on the best individual (Wang & Wang 2025); UTFSBOA fuses directional search and adaptive/nonlinear density factors, a Harris-Hawk-inspired escape-energy factor, and a target-position Cauchy–Gaussian crossover (Wang, Wei & Li 2025); ORSBOA embeds optimal neighborhood perturbation with reverse learning (Chen et al. 2025); CSBOA integrates logistic-tent chaotic initialization, an improved differential mutation operator, and crossover strategies (Mai et al. 2025); and ASBOA adds differential collaborative search, optimal boundary control, and information-retention mechanisms (Meng et al. 2025). None of these variants has been applied to a potential-field inverse problem, and, to the best of our knowledge, SBOA-GI is the first SBOA redesign conceived specifically for gravity inversion, with each modification targeted at the ill-posedness, unequal parameter sensitivity, and depth–amplitude trade-off characteristic of gravity data rather than at generic benchmark performance.

Beyond PSO: the diversification of metaheuristics in potential-field inversion. PSO and its variants remain the most widely applied swarm optimizers in gravity interpretation — tuned PSO for residual gravity anomalies (Roshan & Singh 2017), PSO for fault inversion (Toushmalani 2013a), a constrained adaptive weighted PSO for dipping-fault parameter estimation in which the top- and bottom-layer depths are the most sensitive parameters (Su et al. 2025), and a hybrid PSO–gravitational search algorithm that couples GSA's exploratory strength with PSO's exploitation capacity and augments the recovered model with confidence intervals, histograms, and correlation-based uncertainty analysis (Kumar et al. 2024). The applied literature has broadened considerably, with reviews of metaheuristic-based potential-field inversion reporting stable results from ant colony, cuckoo search, differential evolution, simulated annealing, and bat algorithms applied to gravity and potential-field data (Elhussein et al. 2023); cuckoo optimization adapted to fault gravity inversion (Saibi & Toushmalani 2015); an improved adaptive differential evolution with multiplicative regularization applied to gravity data (Cheng et al. 2023); Hunger Games Search applied to gravity anomalies in geothermal and volcanic settings (Su et al. 2024); a hybrid

metaheuristic scheme proposed for gravity inversion (Hosseinzadeh, Göktürkler & Turan-Karaoğlan 2024); a modified barnacles mating optimizer applied to self-potential anomalies of ore deposits (Ai et al. 2024); and a bat-based global optimizer applied to magnetic data (Essa & Diab 2022). Early comparative studies even reported that PSO produced better agreement with the observed anomaly for fault models than classical linearized Levenberg–Marquardt inversion (Toushmalani 2013b) — a claim that the field-data results of the present study (Section 4.2) usefully qualify.

Adaptive mechanisms, regularization, and non-uniqueness. The individual components of SBOA-GI have precedents in the inversion literature, although their combination, and their assembly around an SBOA core, is new. Multiplicative normalization in adaptive DE removes the need to hand-tune a regularization weight (Cheng et al. 2023); L2 regularization with penalty constraints materially improves inversion stability in weighted-PSO fault inversion, the depth parameters being the dominant contributors to the error (Su et al. 2025); and horizontal-gradient pre-filtering has been shown to improve fault-parameter recovery by reducing the complexity of the parameter space (Elhussein et al. 2023). The depth–amplitude ambiguity that dominates the Charak results has long been documented for the very unified shape-factor expression used here: joint optimization of the shape factor together with other model parameters yields families of near-equivalent solutions in which the amplitude coefficient is strongly tied to the assumed shape (q = 1.5 for a sphere, 1.0 for a horizontal cylinder, 0.5 for a vertical cylinder) (Biswas 2015), and fast interpretation methods for simple bodies operate on the same expression, estimating depth, shape factor, and amplitude coefficient successively (Essa 2007, 2012). These precedents reinforce the methodological stance adopted throughout this paper: a single best model reported without uncertainty context overstates the resolving power of surface gravity data.

2. Methodology

2.1 Forward models

Three idealized causative-body geometries were used, standard in the gravity-inversion literature. For a semi-infinite dipping fault block extending from depth z1 to z2 beneath a step at horizontal position x0, with density contrast Δρ, the vertical gravity effect along a profile follows the classical closed-form expression (Telford, Geldart & Sheriff 1990):

$$g(x) = 2G\Delta\rho \left[z_2 \cdot \arctan(z_2/(x-x_0)) - z_1 \cdot \arctan(z_1/(x-x_0)) + (x-x_0)/2 \cdot \ln\{[(x-x_0)^2+z_2^2]/[(x-x_0)^2+z_1^2]\} \right]$$

This implementation assumes a vertical fault plane (dip = 90°); extension to an arbitrary dip angle is a straightforward addition left for future work rather than folded into the present parameter set.

For a sphere or a horizontal cylinder, both are captured by a single unified expression with a shape factor q (Essa 2007):

$$g(x) = A \cdot z / [(x-x_0)^2+z^2]^q, \; q = 1.5 \text{ (sphere)}, \; q = 1.0 \text{ (horizontal cylinder)}$$

where A absorbs the body's radius and density-contrast terms into a single amplitude parameter, following common practice when the two are not separately resolvable from surface data alone. We note explicitly that our implementation initially labeled the q = 1.0 case a "vertical cylinder"; this was a naming error relative to the standard convention (vertical cylinder corresponds to q = 0.5), and we use the correct term — horizontal cylinder — throughout this paper.

For the areal Charak dataset, which consists of scattered (x, y) stations rather than a single profile, the sphere model was extended radially:

$$g(x,y) = A \cdot z / [(x - x_0)^2 + (y - y_0)^2 + z^2]^{1.5}$$

with (x0, y0) now the map-view coordinates of the source.

2.2 Objective function

All four algorithms minimized the same multiplicative-normalized, L1-norm misfit,

$$\Phi(m) = \Sigma |g_{obs}(x_i) - g_{calc}(x_i, m)| / \Sigma |g_{obs}(x_i)|$$

chosen over an L2 form for two reasons: it removes the need to hand-tune a regularization weight, and its lower sensitivity to isolated outliers is preferable for field data that may carry uncorrected instrument spikes or residual terrain effects.

2.3 SBOA-GI

SBOA-GI retains the three-phase hunting structure and the predator-evasion phase of the original SBOA (Fu et al. 2024) but modifies six components, each targeted at a specific weakness identified when applying the base algorithm to potential-field inversion rather than to generic benchmark functions.

Initialization. Instead of uniform random sampling, the population is built from Latin-hypercube sampling (LHS) over [lb, ub], doubled through opposition-based learning — for every sampled point Xi the reflected point Xi' = lb + ub−Xi is also evaluated, and the fitter half of the combined set is retained. A further 20% of the population is reseeded around a coarse source-location estimate obtained from the station where the observed anomaly's horizontal gradient is largest — a simplified proxy for Euler deconvolution rather than a full implementation.

Hunting phase 1 (t < T/3) replaces SBOA's fixed-scale differential update with a self-adaptive one, xnew = xi + Fi(xr1 − xr2), where the mutation scale Fi for each individual is increased by 5% after a successful update and decreased by 5% otherwise, bounded to [0.1, 0.9].

Hunting phase 2 (T/3 ≤ t<2T/3) reweights the Lévy-flight step per parameter according to a numerically estimated local sensitivity of the objective function around the current best solution, with depth and amplitude parameters — shown by our own sensitivity estimates to dominate the objective — receiving proportionally finer steps than weakly resolved parameters.

Hunting phase 3 (t ≥ 2T/3) monitors the best-fitness trace for stagnation over the preceding 8 iterations; once the change falls below a small threshold, the Lévy step is swapped for a heavier-tailed Cauchy step, giving the search a better chance of escaping a shallow local basin.

Predator-evasion phase. The exploitative branch is clipped to the physical bound box at every update, and whenever a candidate improves on its parent, a short (15-evaluation) bound-constrained Levenberg–Marquardt polish is applied with 30% probability — cheap enough not to dominate the evaluation budget, frequent enough to sharpen convergence near a promising basin.

Outer restart loop. The three-phase cycle is repeated for three rounds; after each round the search bounds are recentered on the current global best and shrunk by a factor of 0.5, reducing dependence on a wide, uninformative initial bracket.

2.4 Baseline algorithms

Standard SBOA was implemented directly from the update equations reported by Fu et al. (2024), with equal population size and three times the per-round iteration budget of SBOA-GI so both receive a comparable number of function evaluations once the outer loop is accounted for. PSO used the canonical constriction-coefficient form (w = 0.729, c1 = c2=1.49). LM inversion used SciPy's bound-constrained trust-region-reflective least-squares solver, started from a uniformly random point within the same bounds as the metaheuristics, run once per trial without restart or multistart — a deliberately "vanilla" baseline, since the comparison is meant to test whether SBOA-GI's added machinery earns its cost against the simplest reasonable classical alternative.

2.5 Experimental protocol

Synthetic tests used three forward models (fault, sphere, horizontal cylinder), each corrupted with 0%, 5%, and 10% Gaussian noise scaled to the clean signal's standard deviation, with 30 independent runs per algorithm–noise combination (population size = 25, matched evaluation budgets). Real-data tests used the residual Bouguer anomaly obtained after removing a second-order polynomial regional trend from the 875-station Charak survey, applied separately to the two most negative local anomalies in the residual field, again with 30 independent runs per algorithm. Because true parameter values are unknown for the field case, performance there was judged by data-space RMS misfit and by run-to-run stability of the recovered parameters rather than by parameter-space RMSE.

2.6 Software and use of AI assistance

All forward models, the four inversion algorithms, and the experiment-execution scripts were implemented in Python (NumPy, SciPy). Portions of this implementation were developed with the assistance of a large language model (Claude, Anthropic) under direct author supervision; every numerical result reported in this paper was produced by independently executing the resulting code, not generated or estimated by the language model itself. AI assistance was also used in drafting and organizing manuscript text, which the author reviewed, edited, and takes full accountability for.

3. Synthetic Validation

3.1 Fault model

Table 1 summarizes parameter-space RMSE across 30 independent runs of each algorithm at three noise levels for the vertical-fault model (true parameters: x0 = 500 m, z1 = 50 m, z2 = 300 m, Δρ = 0.35 g/cc).

Table 1
Fault-model inversion statistics, mean ± std over 30 runs.

Algorithm	Noise	RMSE (mean ± std)	Mean evals	Mean CPU (s)
SBOA-GI	0%	4.9e-12 ± 8.7e-12	10034	0.60
SBOA	0%	1.236 ± 1.313	9025	0.26
PSO	0%	5.100 ± 8.620	4525	0.08
LM	0%	10.358 ± 39.417	15	0.004
SBOA-GI	5%	4.020 ± 0.530	11440	1.03
SBOA	5%	4.035 ± 1.220	9025	0.28
PSO	5%	8.110 ± 9.961	4525	0.09
LM	5%	4.410 ± 0.000	15	0.005
SBOA-GI	10%	6.840 ± 0.846	11526	1.10
SBOA	10%	6.620 ± 1.994	9025	0.29
PSO	10%	18.128 ± 16.503	4525	0.08
LM	10%	13.389 ± 26.810	13	0.004

At 0% noise, SBOA-GI's shrinking-bound restart loop and embedded LM polish drive the parameter RMSE roughly eleven orders of magnitude below standard SBOA — visible in Fig. 2 as three successive step-drops in the convergence curve, one per outer round. At 5% noise the margin over standard SBOA nearly vanishes (4.02 vs. 4.04), and at 10% noise the ranking inverts: standard SBOA (6.62) is marginally better than SBOA-GI (6.84). We interpret this as evidence that once measurement noise sets a floor on achievable misfit, SBOA-GI's extra machinery — designed to refine a solution once it is close to the true optimum — has nothing further to exploit and instead risks fitting noise rather than signal. PSO trails both SBOA variants at every noise level, and unconstrained single-start LM shows the largest variance of all four methods at 0% and 10% noise, consistent with its known vulnerability to poor initial guesses; at 5% noise, by contrast, LM converges to an essentially identical, highly stable solution on every run, discussed further in Section 6. Full convergence curves at 5% and 10% noise and the corresponding RMSE boxplots are provided as Fig. S1–S3 (Online Resource 1).

3.2 Sphere and horizontal-cylinder models

Because the sphere and cylinder parameter vectors mix quantities of very different physical scale (position and depth in meters vs. an amplitude term of order 10^6), raw parameter-space RMSE is dominated by the amplitude term and is not a physically meaningful summary statistic for these two models; we report per-parameter relative error instead (Table 2).

Table 2
Mean relative error (%) per parameter, sphere and horizontal-cylinder models, 30 runs.

Model	Algorithm	Noise	x0 err %	z err %	A err %
Sphere	SBOA-GI	0%	0.000	0.000	0.000
Sphere	SBOA-GI	5%	0.039	1.176	1.116
Sphere	SBOA-GI	10%	0.057	2.271	2.095
Sphere	SBOA	10%	0.058	2.299	2.135
Sphere	PSO	10%	0.050	2.277	2.091
Sphere	LM	10%	0.308	1.595	2.518
Cylinder	SBOA-GI	10%	0.190	3.006	0.624
Cylinder	SBOA	10%	0.183	2.988	0.606
Cylinder	PSO	10%	0.159	2.920	0.537
Cylinder	LM	10%	0.334	1.777	1.129

For both simple-body models, all three population-based algorithms reach essentially exact recovery at 0% noise and remain within roughly one percentage point of each other at every noise level tested. SBOA-GI shows no measurable advantage over standard SBOA or PSO for either geometry, and is 2–5 times more computationally expensive. This is a materially different outcome from the fault model and is, in our reading, attributable to the shape of the two problems' misfit surfaces: the fault model's four parameters interact non-linearly through the arctan/log kernel and its noise-free misfit surface retains sharper local structure that rewards SBOA-GI's shrinking-bound refinement, whereas the sphere/cylinder kernel is smoother and closer to convex over the tested bounds, leaving little for any of the three metaheuristics to improve upon relative to one another (Fig. 3; full RMSE distributions in Fig. S4–S5, Online Resource 2–3).

4. Field Application: Charak Salt-Dome Anomalies, Zagros, Iran

4.1 Study area and data

The Charak survey area lies within the eastern Fars salt-diapir province of the Zagros fold-and-thrust belt, a region hosting one of the world's densest concentrations of exposed and buried salt structures rooted in the Neoproterozoic–Cambrian Hormuz Series, which typically comprises halite intermixed with gypsum, dolomite, and minor volcanic rock and rises through the overlying sedimentary sequence under buoyancy forces because of its low density relative to the surrounding formations (Jahani et al. 2007). The stratum density table accompanying the dataset is consistent with this contrast: the lightest unit listed (1.92 g/cc) sits well below the denser units expected in the overburden (2.19–2.52 g/cc), supporting the expectation of a negative gravity signature over any shallow salt body in the survey.

The dataset comprises 875 Bouguer-anomaly stations acquired along irregularly spaced north–south lines spanning roughly 58 km (E–W) by 27 km (N–S), with observed values ranging from − 51.7 to − 38.4 mGal (Fig. 4). A second-order polynomial trend surface was fitted and removed to isolate the shorter-wavelength residual attributable to shallow structure (Fig. 5); we note this as a standard but relatively simple regional–residual separation and return to its limitations in Section 6. The residual field contains two distinct negative closures, hereafter Dome 1 (centered near UTM x ≈ 213,700, y ≈ 2,962,500; residual minimum − 7.60 mGal) and Dome 2 (near x ≈ 196,000, y ≈ 2,960,500; residual minimum − 6.27 mGal), each treated as an independent single-source inversion target using the areal sphere model of Section 2.1, with stations restricted to a 6 km half-window around each closure (102 and 52 stations respectively) and search bounds of $z \in [100, 3000]$ m, $A \in [-5\times10^{7}, -10^{2}]$ (negative amplitude enforced by the known sign of the density contrast).

4.2 Inversion results

Table 3
Real-data inversion statistics, mean ± std over 30 runs, sphere model.

Target	Algorithm	RMS misfit (mGal)	Depth z (m)	Mean CPU (s)
Dome 1	LM	2.155 ± 2.4e-9	1608 ± 0.2	0.006
Dome 1	SBOA	2.186 ± 7.6e-4	2219 ± 8.5	0.21
Dome 1	SBOA-GI	2.186 ± 1.0e-3	2228 ± 10.2	2.05
Dome 1	PSO	2.199 ± 1.3e-2	2628 ± 372	0.06
Dome 2	LM	1.249 ± 4.3e-9	2581 ± 0.1	0.007
Dome 2	SBOA	1.282 ± 1.4e-5	2774 ± 0.4	0.22
Dome 2	SBOA-GI	1.282 ± 1.6e-4	2774 ± 2.8	2.06
Dome 2	PSO	1.282 ± 3.4e-9	2774 ± 0.00001	0.06

Two results stand out and both run against our initial expectation. First, classical LM achieved the lowest and among the most stable misfit for both targets, at 1/300th to 1/30th of the metaheuristics' computational cost. Second, the depth estimates from LM are markedly shallower than those from the

three population-based methods for Dome 1 (1608 m vs. ≈2200–2600 m) despite LM achieving the better data fit — a clear signature of the classical depth–amplitude ambiguity in potential-field inversion, discussed in Section 6, rather than of any algorithm converging to a "wrong" answer in an absolute sense. For Dome 2, the amplitude parameter A pinned at its lower bound in the majority of SBOA, SBOA-GI and PSO runs, indicating the search was pushing against, and possibly limited by, the physical bound we imposed. The corresponding fit map for Dome 2 is provided as Fig. S6; complete per-run results for both domes are available as Online Resource 4–5.

Figure 6 compares the observed residual field, the best-fit calculated field, and the spatial misfit pattern for Dome 1. The calculated field reproduces the location and approximate magnitude of the negative closure, but the observed field carries a north–south elongation that the single-point-source sphere model cannot reproduce, leaving a systematic misfit pattern rather than pure random residual. RMS misfit for both domes (2.16 and 1.25 mGal) corresponds to roughly 15–20% of the respective peak-to-peak residual anomaly amplitude, a moderate, physically plausible but clearly improvable fit for a four-parameter single-body approximation of what is, in reality, a geologically complex, elongated, and — as the two separate closures themselves demonstrate — multi-body structure.

Figure 7 shows the mean estimated source center and a depth-scaled footprint circle for each algorithm, overlaid on both anomalies; the four algorithms' solutions cluster tightly in map-view position, while depth (and hence footprint size) diverges most for LM relative to the three metaheuristics on Dome 1.

5. Discussion

Taken together, the synthetic and field results tell a more nuanced story than either a straightforward "our method wins" or "our method fails" narrative would suggest, and we think the nuance itself is the more useful finding for practitioners choosing among these tools.

On the fault model, SBOA-GI's redesigned initialization and shrinking-bound restart loop delivered a real, large, and reproducible gain — but only in the noise-free case, where there is an exact answer to converge to and enough iterations to reach it. Once 5% noise was added, that gain collapsed to a rounding error, and at 10% noise the plain SBOA baseline nosed ahead. We think the honest reading of this is not that SBOA-GI "stopped working," but that its refinement machinery is solving a problem — squeezing the last few significant digits out of a solution — that measurement noise had already rendered moot. A local LM polish, however well-timed, cannot recover information the data do not contain.

The sphere and horizontal-cylinder results reinforce this reading from a different angle: here even standard SBOA and PSO reached near-exact recovery at zero noise, so there was essentially no residual error left for SBOA-GI's extra mechanisms to reduce, and the added cost bought nothing. This matches the broader pattern in the SBOA-variant literature reviewed in Section 1 — improvements measured on generic benchmark functions do not automatically transfer to a specific applied inverse problem, and

whether they transfer seems to depend heavily on how much exploitable structure the particular objective surface still has once the easy part of the search is done.

The field results push this point further than we expected going in. We had designed SBOA-GI anticipating that a real, noisy, structurally imperfect dataset would be exactly the regime where a hybrid global–local scheme should shine relative to a single-start gradient method prone to local-minimum capture. Instead, LM converged fastest, most cheaply, and to the lowest misfit on both Charak anomalies. Figure 7 shows why this is plausible rather than anomalous: the four algorithms' mean solutions cluster tightly in map-view position for both domes, meaning the horizontal location of each source is well constrained by the data and easy for any reasonable optimizer to find — there is no field of scattered local minima here for a global search to earn its keep against. What differs across algorithms is depth and amplitude, and that difference is a signature of trade-off along a single elongated valley in parameter space rather than of separate, competing basins (Section 6). A gradient method that starts inside or near that valley walks straight down it; a population-based method spreads its evaluation budget across the whole valley and the surrounding search box, which is the right behavior when there might be multiple basins but is simply less efficient when there is really only one.

6. Non-Uniqueness and Limitations

Depth–amplitude trade-off. For a source approximated as a point mass or line mass, the surface field scales as $Az/(r^2+z^2)q$; increasing z and increasing |A| in the right proportion leaves the field at the peak nearly unchanged while broadening its shoulders only slightly, so a wide range of (z, A) pairs fit the same data almost equally well. This is a textbook non-uniqueness of potential-field inversion (Blakely 1995), not a defect of any algorithm tested here, and it is visible directly in our own results: for Dome 1, LM's depth (1608 m) and the metaheuristics' depth (≈ 2200–2600 m) differ by 40–60% while their data misfits differ by less than 3%. Reporting a single "best" depth without this caveat, as much of the applied literature implicitly does by presenting only the winning run, would overstate the resolving power of the survey. For Dome 2, several runs of SBOA, SBOA-GI, and PSO pinned the amplitude at the imposed lower bound, which is itself evidence that the true optimum may lie beyond the physically motivated range we selected, or that the trade-off valley is even less curved for that anomaly than for Dome 1 — we did not widen the bound and re-run to chase a better-looking number, since doing so after seeing the result would be exactly the kind of post-hoc adjustment the golden rule of this project was meant to prevent.

Single-source approximation of a multi-source field. Both Charak anomalies were inverted independently with a single-sphere model, while the residual map (Fig. 5) shows two separate closures within the same survey and, within each closure, a misfit pattern (Fig. 6, right panel) with spatial structure rather than pure noise. A simultaneous multi-source inversion — one parameter vector spanning both domes' positions, depths, and amplitudes under a shared objective function — would let the field of one dome influence the fitted parameters of the other in a physically consistent way, and is a natural next step; we did not attempt it here because doubling the parameter count changes the

character of the search problem enough that it deserves its own dedicated comparison rather than a rushed add-on to this one.

Regional–residual separation. The second-order polynomial trend used to isolate the residual field is a coarse, commonly used but non-unique choice; a different trend order, or a wavelength-based method such as upward continuation, would produce a measurably different residual and, in turn, different inversion results. The elongated, non-circular character of the observed residual noted in Section 4.2 is at least partly attributable to this step rather than purely to subsurface geometry, and we would not want a reader to over-interpret the north–south elongation as necessarily geological.

Vertical-fault simplification. The fault forward model assumes a 90° dip; real Zagros structures associated with salt movement are commonly non-vertical, and the true fault geometry, where relevant to a given field target, would require either a dipping-fault kernel or an additional free dip parameter, neither of which was implemented here.

Simplified initial-guess seeding. The gradient-based seed used in SBOA-GI's initialization is a maximum-horizontal-gradient proxy, not a full Euler deconvolution solution for structural index and depth. A proper Euler deconvolution implementation would likely produce a tighter, more informative initial bracket and could change the relative standing of SBOA-GI in future tests; we flag this as an implementation gap rather than a methodological choice we stand behind.

7. Conclusion

We set out to test whether a purpose-built, physics-informed redesign of a recent metaheuristic — the Secretary Bird Optimization Algorithm — earns a genuine advantage over its unmodified form, over PSO, and over classical Levenberg–Marquardt inversion, when applied to gravity data rather than generic optimization benchmarks. The answer is conditional rather than uniformly favorable to our own method, which we take to be the more scientifically useful outcome to report. SBOA-GI's combination of structured initialization, adaptive mutation, sensitivity-weighted step control, a Lévy–Cauchy stagnation escape, and an embedded local LM polish produced an eleven-order-of-magnitude accuracy gain over standard SBOA on a noise-free, structurally complex fault model, but that advantage narrowed to negligible at 5% noise and reversed at 10% noise, and was not reproduced at all on the simpler sphere and horizontal-cylinder geometries. On real Charak salt-dome gravity data, classical LM — the simplest and cheapest method tested — produced the best and most stable fit for both anomalies studied, a result we attribute to the smooth, weakly multimodal character of the misfit surface for a well-located single source rather than to any shortcoming specific to the metaheuristics. Where SBOA-GI's added machinery has clear practical value is convergence speed on harder, noise-free problems, not final accuracy on noisy or already-smooth ones — a distinction that matters for anyone deciding whether the extra implementation and runtime cost is worth paying for a particular field problem.

Declarations

Competing Interests:

The author has no competing interests to declare that are relevant to the content of this article.

Funding:

The author did not receive support from any organization for the submitted work. No funding was received to assist with the preparation of this manuscript.

Author Contribution

This is a single-author work. The author was solely responsible for all stages of the study, including conceptualization, methodology design, software implementation, formal analysis and investigation, data curation, and writing of the original draft and all revisions, and approved the final manuscript.

Data Availability:

The complete per-run numerical results underlying all summary statistics in this article are provided as supplementary spreadsheets (Online Resource 1–5). The Charak gravity dataset, stratum density table, and all analysis/algorithm source code are available from the corresponding author on reasonable request.

References

1. Ai H, Ekinci YL, Balkaya Ç, Alvandi A, Ekinci R, Roy A, Su K, Pham LT (2024) Modified barnacles mating optimizing algorithm for the inversion of self-potential anomalies due to ore deposits. Nat Resour Res 33(3):1073–1102. https://doi.org/10.1007/s11053-024-10331-7
2. Anderson NL, Essa KS, Elhussein M (2020) A comparison study using particle swarm optimization inversion algorithm for gravity anomaly interpretation due to a 2D vertical fault structure. J Appl Geophys 179:104120. https://doi.org/10.1016/j.jappgeo.2020.104120
3. Biswas A (2015) Interpretation of residual gravity anomaly caused by simple shaped bodies using very fast simulated annealing global optimization. Geosci Front 6(6):875–893. https://doi.org/10.1016/j.gsf.2015.03.001
4. Blakely RJ (1995) Potential Theory in Gravity and Magnetic Applications. Cambridge University Press, Cambridge
5. Chen C, Cao L, Chen B, Chen Y, Wu X (2025) A dual-mechanism enhanced secretary bird optimization algorithm and its application in engineering optimization. Biomimetics 10(10):679. https://doi.org/10.3390/biomimetics10100679

6. Cheng L, Xiao T, Hu X, Mohamed AW, Liu Y, Du W (2023) Inversion of gravity data with multiplicative regularization using an improved adaptive differential evolution. Minerals 13(8):1027. https://doi.org/10.3390/min13081027
7. Elhussein M, Abo-Ezz ER, Gomaa OA, Géraud Y, Essa KS (2023) Two-sided fault parameter assessment through the utilization of a particle swarm optimizer to different gravity horizontal gradients-orders with application to various cases studies. Environ Earth Sci 82(21). https://doi.org/10.1007/s12665-023-11081-0
8. Essa KS (2007) A simple formula for shape and depth determination from residual gravity anomalies. Acta Geophys 55:182–190. https://doi.org/10.2478/s11600-007-0003-9
9. Essa KS (2012) A fast interpretation method for inverse modeling of residual gravity anomalies caused by simple geometry. J Geol Res 2012:1–10. https://doi.org/10.1155/2012/327037
10. Essa KS, Diab ZE (2022) An automatic inversion approach for magnetic data applying the global bat optimization algorithm (GBOA): application to ore deposits and basement rock intrusion. Geomechanics and Geophysics for Geo-Energy and Geo-Resources 8(6). https://doi.org/10.1007/s40948-022-00492-1
11. Fu Y, Liu D, Chen J, He L (2024) Secretary bird optimization algorithm: a new metaheuristic for solving global optimization problems. Artif Intell Rev 57(5):123. https://doi.org/10.1007/s10462-024-10729-y
12. Hosseinzadeh S, Göktürkler G, Turan-Karaoğlan S (2024) Inversion of gravity anomalies by a hybrid metaheuristic algorithm. Deu Muhendislik Fakultesi Fen ve Muhendislik 26(78):379–388. https://doi.org/10.21205/deufmd.2024267804
13. Jahani S, Callot J-P, Frizon de Lamotte D, Letouzey J, Leturmy P (2007) The Salt Diapirs of the Eastern Fars Province (Zagros, Iran): A Brief Outline of their Past and Present. In: Lacombe O, Lavé J, Roure F, Vergés J (eds) Thrust Belts and Foreland Basins. Springer, Berlin, Heidelberg, pp 289–308. https://doi.org/10.1007/978-3-540-69426-7_15
14. Kumar N, Sarkar K, Singh UK (2024) Gravity data inversion for parameters assessment over geologically faulted structures—a hybrid particle swarm optimization and gravitational search algorithm technique. Geophys Prospect 73(1):188–212. https://doi.org/10.1111/1365-2478.13638
15. Levenberg K (1944) A method for the solution of certain non-linear problems in least squares. Q Appl Math 2(2):164–168
16. Mai X, Zhong Y, Li L (2025) The crossover strategy integrated secretary bird optimization algorithm and its application in engineering design problems. Electron Res Archive 33(1):471–512. https://doi.org/10.3934/era.2025023
17. Marquardt DW (1963) An algorithm for least-squares estimation of nonlinear parameters. J Soc Ind Appl Math 11(2):431–441
18. Meng Q, Kuang X, Yu Z, He M, Cui H (2025) Augmented secretary bird optimization algorithm for wireless sensor network deployment and engineering problem. PLoS ONE 20(8). https://doi.org/10.1371/journal.pone.0329705

19. Qin H, Yang S, Liu Z, Li G (2024) An improved secretary bird optimization algorithm. Proc. Int. Symp. Power Electronics, Distributed Generation Systems (ISPDS) 442–445. https://doi.org/10.1109/ispds62779.2024.10667529
20. Roshan R, Singh UK (2017) Inversion of residual gravity anomalies using tuned PSO. Geoscientific Instrumentation. Methods Data Syst 6(1):71–79. https://doi.org/10.5194/gi-6-71-2017
21. Saibi H, Toushmalani R (2015) Gravity inversion of a fault by Cuckoo optimization. Near-Surface Asia Pacific Conference, Waikoloa, Hawaii, 7–10 July 2015, 1:196–199. https://doi.org/10.1190/nsapc2015-052
22. Su K, Ai H, Alvandi A, Lyu C, Wei X, Qin Z, Tu Y, Yan Y, Nie T (2024) Hunger Games Search for the elucidation of gravity anomalies with application to geothermal energy investigations and volcanic activity studies. Open Geosci 16(1). https://doi.org/10.1515/geo-2022-0641
23. Su S-Q, Liang J, Xu C, Zhang F, Yu H (2025) Constrained adaptive weighted particle swarm optimization (C-AWPSO) algorithm for dipping fault parameter inversion. Appl Sci 15(15):8382. https://doi.org/10.3390/app15158382
24. Telford WM, Geldart LP, Sheriff RE (1990) Applied Geophysics, 2nd edn. Cambridge University Press, Cambridge
25. Toushmalani R (2013) Gravity inversion of a fault by Particle swarm optimization (PSO). SpringerPlus 2(1):315. https://doi.org/10.1186/2193-1801-2-315
26. Toushmalani R (2013b) Comparison result of inversion of gravity data of a fault by particle swarm optimization and Levenberg-Marquardt methods. SpringerPlus 2(1):462. https://doi.org/10.1186/2193-1801-2-462
27. Wang F, Wang B (2025) Multi-strategy improved secretary bird optimization algorithm. J Comput Commun 13(1):90–107. https://doi.org/10.4236/jcc.2025.131007
28. Wang X, Wei P, Li Y (2025) Enhanced secretary bird optimization algorithm with multi-strategy fusion and Cauchy–Gaussian crossover. Sci Rep 15(1):23163. https://doi.org/10.1038/s41598-025-04469-4
29. Yan N, Ding TJ (2025) An improved secretary bird optimization algorithm with hybrid improvement strategies. Proc. SPIE 13561:55. https://doi.org/10.1117/12.3059231

Figures

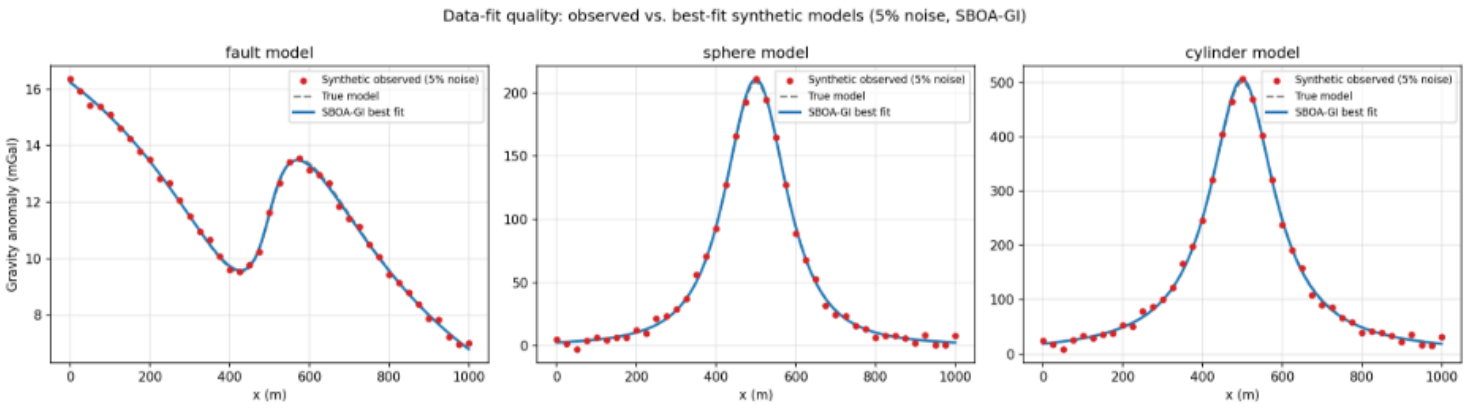


Figure 1

Observed synthetic data (5% noise), true model, and SBOA-GI best fit for the fault, sphere, and horizontal-cylinder forward models.

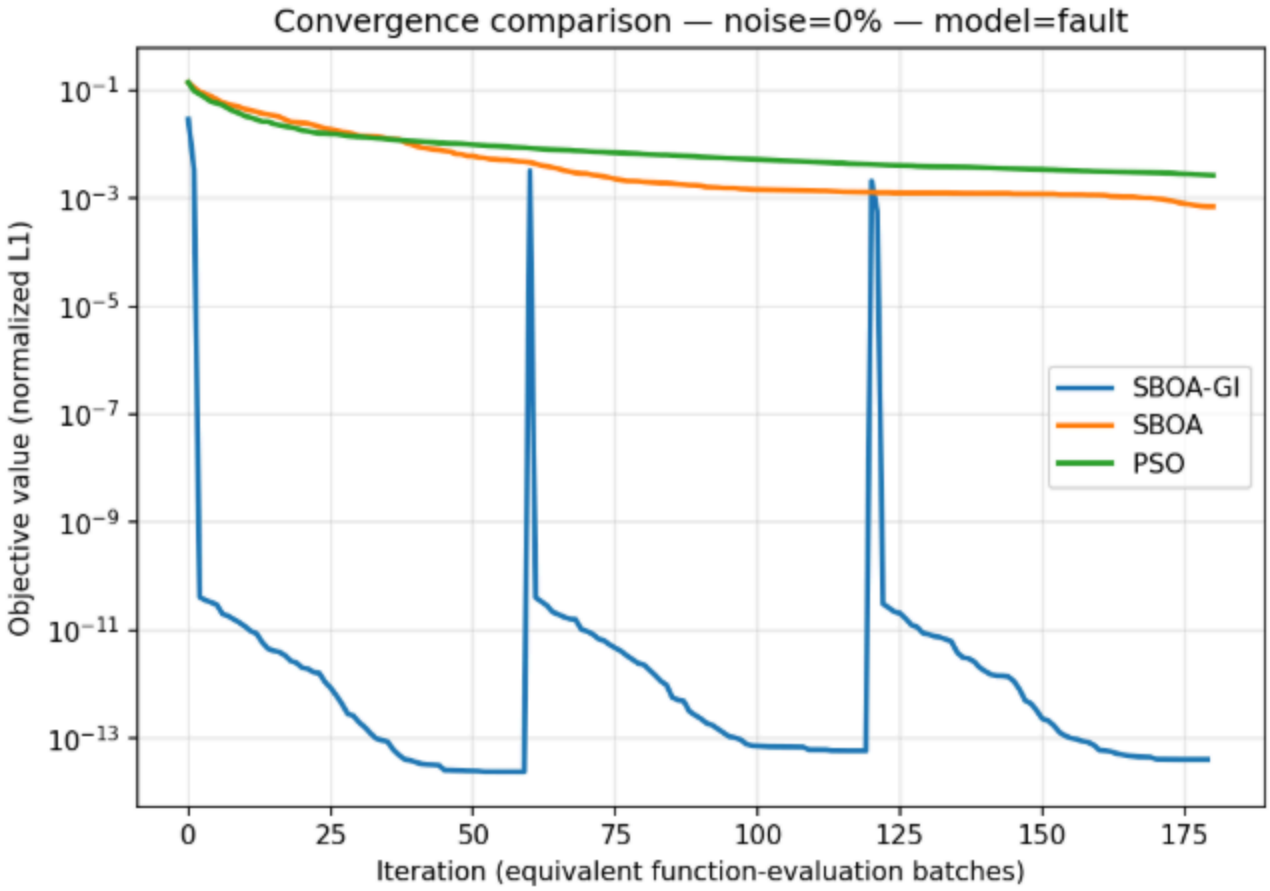


Figure 2

Convergence of SBOA-GI, standard SBOA, and PSO on the noise-free fault model. Step-drops in the SBOA-GI curve correspond to the three outer shrinking-bound restarts.

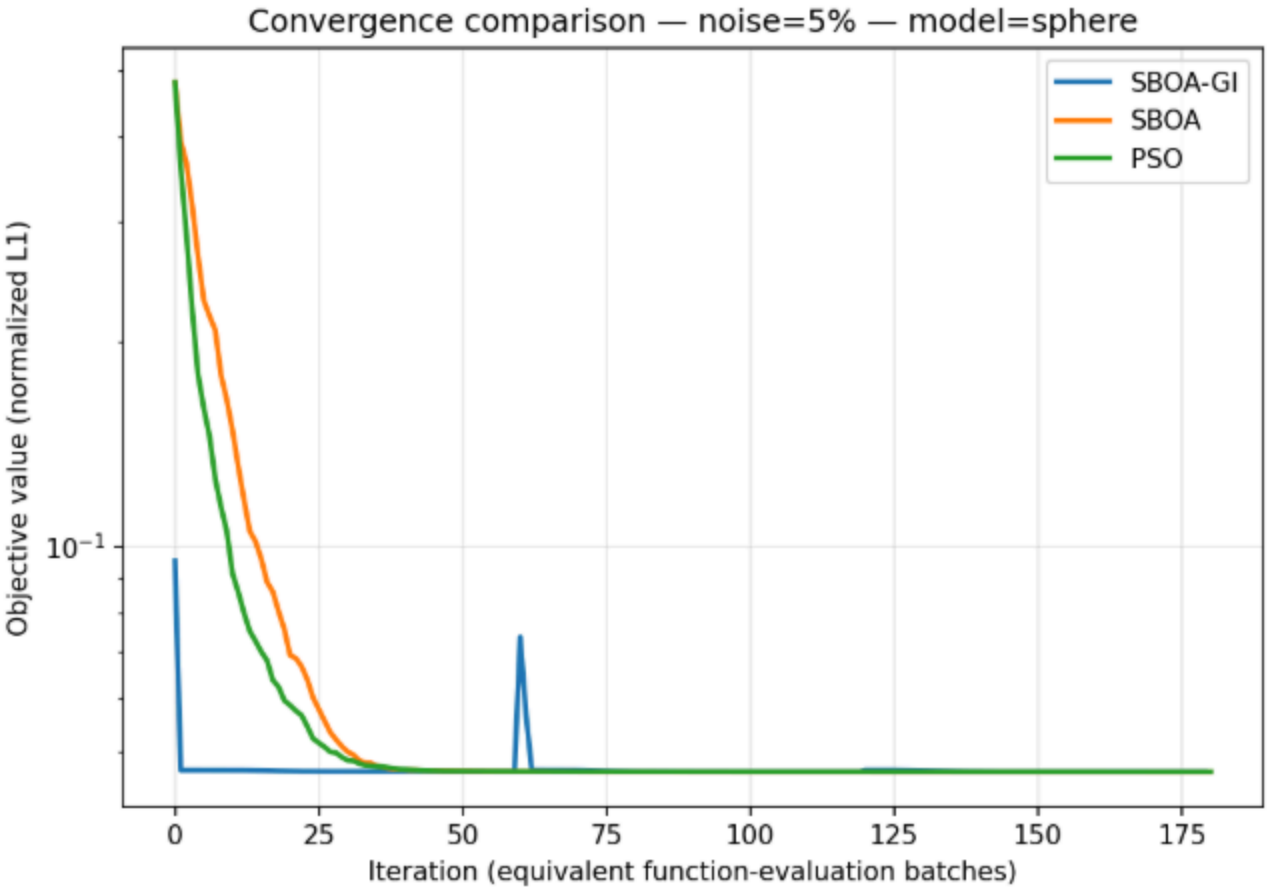


Figure 3

Convergence comparison on the sphere model at 5% noise: SBOA-GI converges fastest but SBOA and PSO reach the same final objective value by iteration ~40.

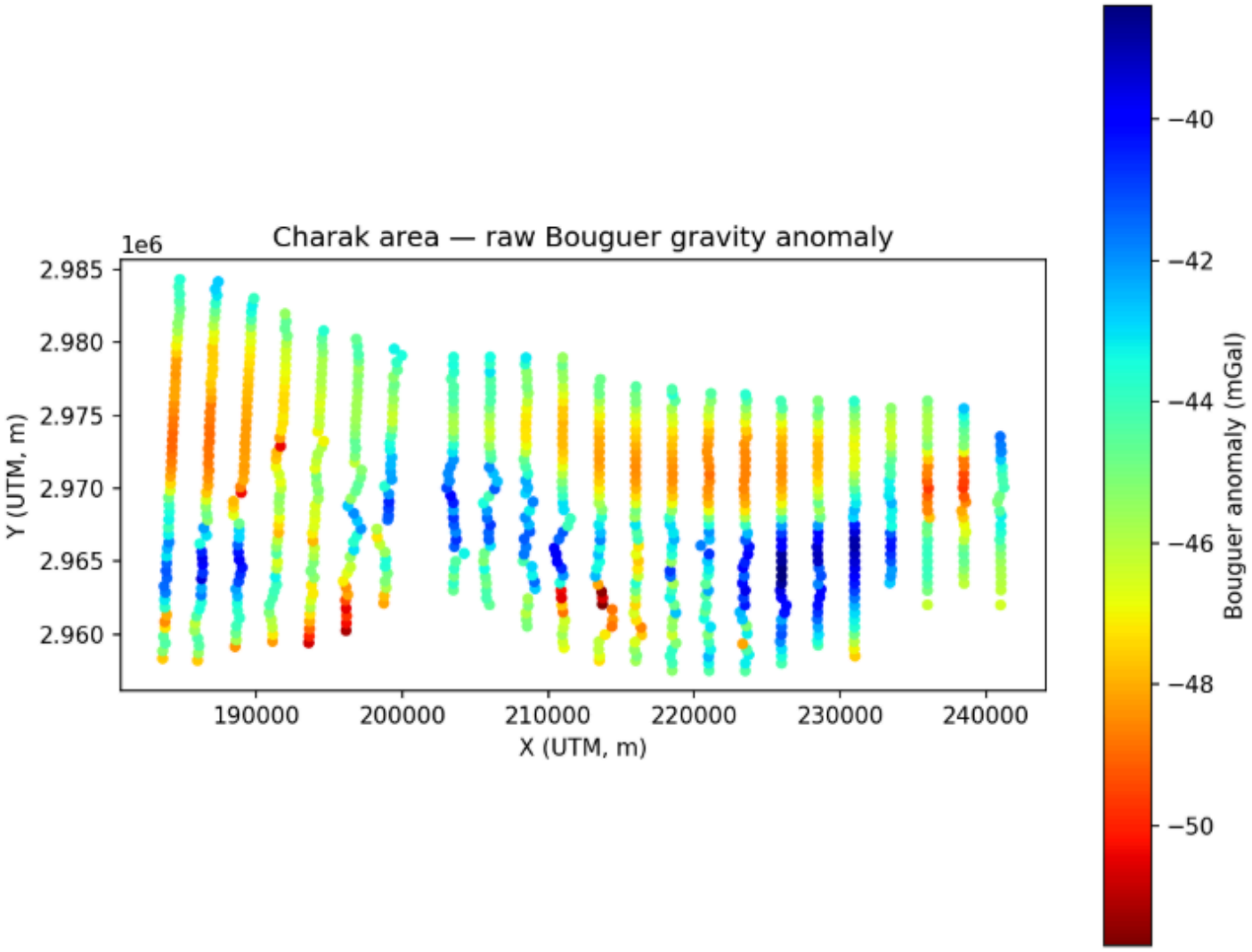


Figure 4

Raw Bouguer gravity anomaly, Charak survey area (875 stations).

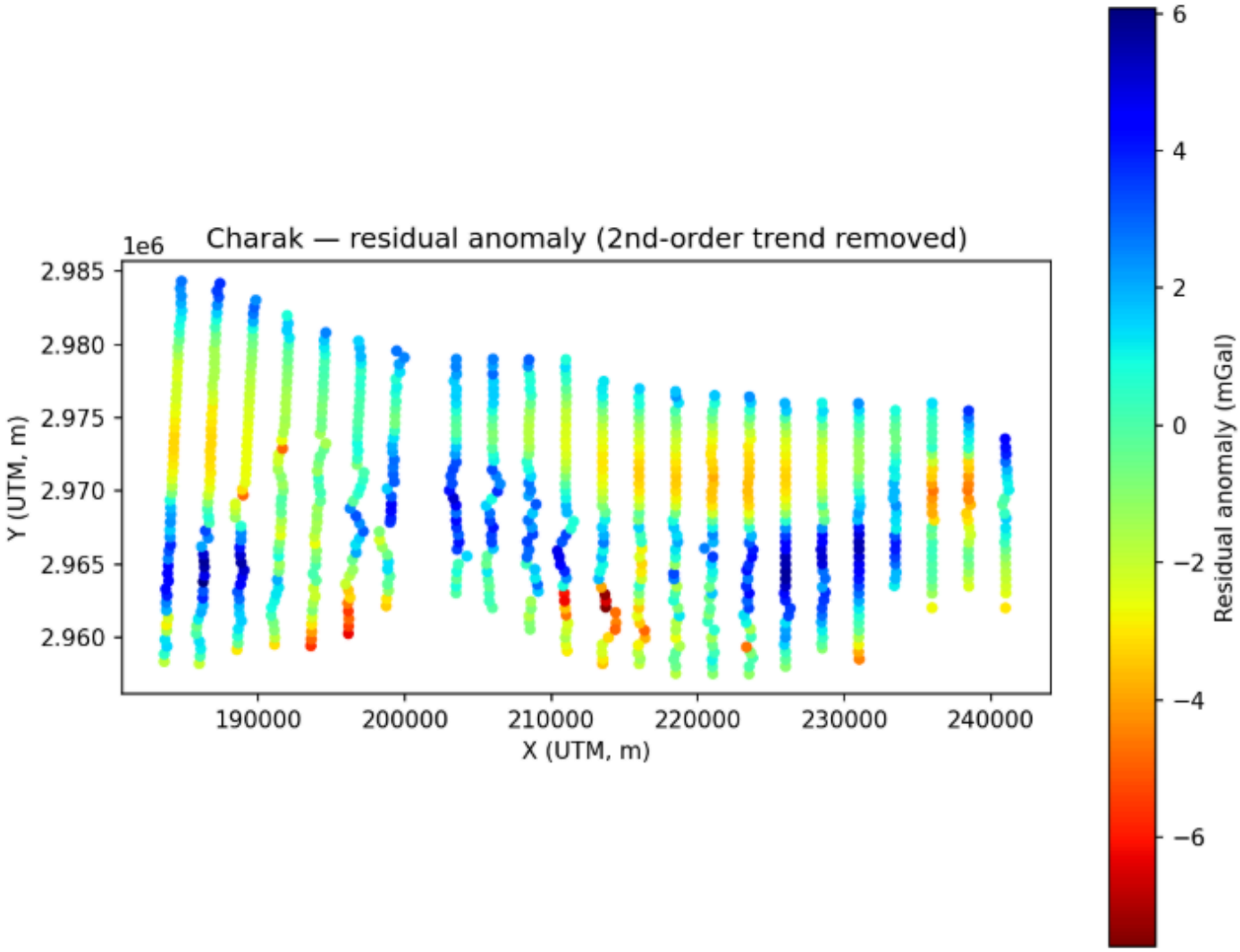


Figure 5

Residual anomaly after removing a second-order regional trend, showing two negative closures (Dome 1, Dome 2).

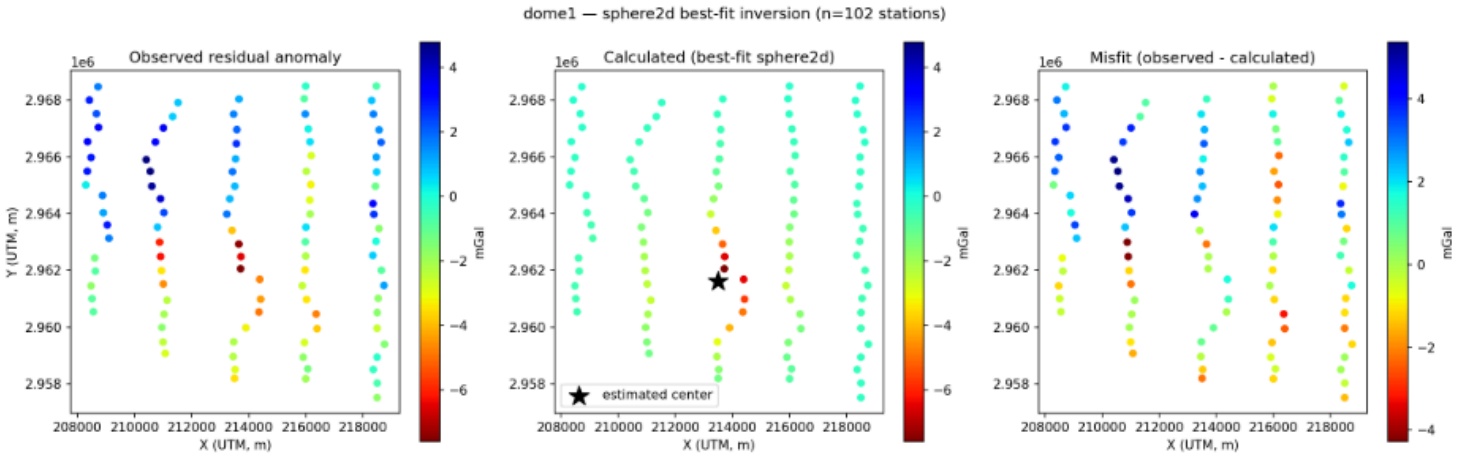


Figure 6

Dome 1: observed residual anomaly, best-fit calculated field, and spatial misfit (observed − calculated).

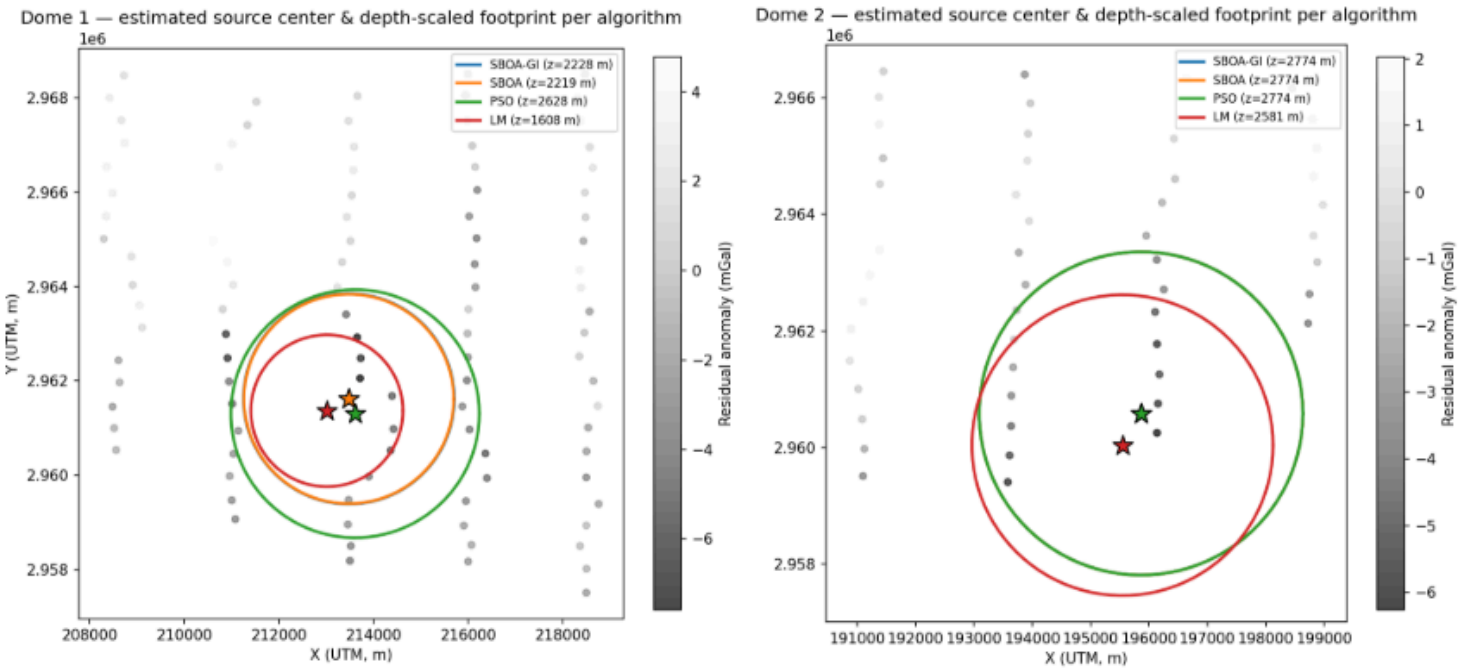


Figure 7

Estimated source center (star) and depth-scaled footprint (circle, radius = estimated depth) per algorithm, for Dome 1 and Dome 2, overlaid on the residual anomaly.

Supplementary Files

This is a list of supplementary files associated with this preprint. Click to download.

- ESM1.csv
- ESM2.csv
- ESM3.csv
- ESM4.csv
- ESM5.csv
- SupplementaryInformation.docx